The Astrophysical Journal, 995:65 (13pp), 2025 December 10 https://doi.org/10.3847/1538-4357/ae11a8

Supersonic Turbulence in Primordial Halos: a Comparison with and without the Stream Velocity

Avi Chen[1], William Lake[2,3], Claire E. Williams[2,3], Blakesley Burkhart[1,4], Smadar Naoz[2,3], Shyam H. Menon[1,4], Federico Marinacci[5,6], Mark Vogelsberger[7], and Naoki Yoshida[8,9,10]
[1] Department of Physics and Astronomy, Rutgers, The State University of New Jersey, 136 Frelinghuysen Road, Piscataway, NJ 08854, USA; avi.chen@rutgers.edu
[2] Department of Physics and Astronomy, UCLA, Los Angeles, CA 90095, USA
[3] Mani L. Bhaumik Institute for Theoretical Physics, Department of Physics and Astronomy, UCLA, Los Angeles, CA 90095, USA
[4] Center for Computational Astrophysics, Flatiron Institute, 162 Fifth Avenue, New York, NY 10010, USA
[5] Department of Physics & Astronomy "Augusto Righi", University of Bologna, via Gobetti 93/2, 40129 Bologna, Italy
[6] INAF, Astrophysics and Space Science Observatory Bologna, Via P. Gobetti 93/3, I-40129 Bologna, Italy
[7] Department of Physics and Kavli Institute for Astrophysics and Space Research, Massachusetts Institute of Technology, Cambridge, MA 02139, USA
[8] Department of Physics, The University of Tokyo, 7-3-1 Hongo, Bunkyo, Tokyo 113-0033, Japan
[9] Kavli Institute for the Physics and Mathematics of the Universe (WPI), UT Institute for Advanced Study, The University of Tokyo, Kashiwa, Chiba 277-8583, Japan
[10] Research Center for the Early Universe, School of Science, The University of Tokyo, 7-3-1 Hongo, Bunkyo, Tokyo 113-0033, Japan
Received 2025 July 22; revised 2025 October 2; accepted 2025 October 8; published 2025 December 4

Abstract

Turbulence plays a critical role in regulating star formation in molecular clouds and is also observed in simulations of primordial halos that host Population III (Pop III) stars. The relative velocity between baryons and dark matter at the time of recombination is thought to be a source of turbulence in the early Universe. In this paper, we study how this stream velocity affects the turbulence inside primordial halos using high-resolution cosmological simulations across the redshift range of $z = 30$ to $z = 20$. We find that at a fixed redshift, the stream velocity enhances turbulence in low-mass halos ($M \lesssim 10^6\,M_\odot$) and suppresses it for high-mass halos ($M \gtrsim 10^6\,M_\odot$). The enhancement in low-mass halos likely arises from residual kinetic energy introduced by the stream velocity, while the suppression in high-mass halos likely arises from a reduction in accretion-driven turbulence. This mass-dependent modulation of turbulence suggests that the initial conditions inside primordial halos are altered in the presence of the stream velocity, potentially influencing their fragmentation and the resulting star formation.

Unified Astronomy Thesaurus concepts: Galaxy formation (595); Cosmology (343); Population III stars (1285); Star formation (1569); Hydrodynamical simulations (767); High-redshift galaxies (734)

1. Introduction

For the first ∼380,000 yr after the Big Bang, the Universe was mostly a homogeneous and isotropic plasma containing protons, neutrons, electrons, and photons. The baryons were coupled to the photons via their mutual coupling to the electrons. Slight baryonic overdensities, originally seeded by quantum fluctuations, were therefore prevented from growing gravitationally due to the radiation pressure of the photons. This created a standing wave of matter known as Baryon Acoustic Oscillations (BAO). Since dark matter (DM) does not interact with electromagnetic radiation, it did not experience these oscillations and accelerated gravitationally while coalescing into potential wells. This caused a significant relative velocity between the DM and the baryons. At the time of recombination, $z \sim 1020$, the rate of Thomson scattering dropped dramatically, and the photons kinetically decoupled from the baryons (though they were still somewhat coupled through scattering with the residual uncombined electrons). As a result, the sound speed of the baryons dropped from highly relativistic $\sim c/\sqrt{3}$ to thermal speeds of an ideal gas $\sim 6\,\mathrm{km\,s^{-1}}$. The DM, not being coupled to the radiation, did not experience this negative acceleration. The relative velocity, therefore, became supersonic with (following a Gaussian distribution) rms velocities $\sigma_{\rm vbc} \sim 30\,\mathrm{km\,s^{-1}}$ and a Mach number of $\mathcal{M} \sim 5$ (e.g., D. Tseliakhovich & C. Hirata 2010; D. Tseliakhovich et al. 2011).

Using moving-background perturbation theory, D. Tseliakhovich & C. Hirata (2010) showed the necessity of including the term representing the relative velocity between the baryons and the DM at the time of recombination, despite it being nominally second order. This is because at the scale $k_{vbc} \equiv aH/v_{bc}$, the expansion parameter of this term is of order unity (D. Tseliakhovich et al. 2011). Being ultimately derived from similar physics underlying the BAO, the relative velocity is coherent on the same scales as the Silk damping of a few Mpc and can therefore be numerically modeled as a uniform velocity boost below that scale. The relative velocity, therefore, is often simply called the "stream velocity" or "streaming" and decays, like the peculiar velocity of a free particle, as $a(t)^{-1}$.

The stream velocity alters the formation and observational signatures of early-Universe objects at high redshifts. The spatial offset between baryons and DM generated by the stream velocity acts as an effective anisotropic pressure on the gas (e.g., M. McQuinn & R. M. O'Leary 2012). This has a cascading effect that has been well studied both analytically and numerically (see the review by A. Fialkov 2014). The minimum halo mass required for cooling and the Jeans mass is increased, delaying the formation of Population III stars (Pop III; e.g., T. H. Greif et al. 2011; U. Maio et al. 2011; A. Stacy et al. 2011; A. Fialkov et al. 2012; S. Naoz et al. 2012, 2013; C. Popa et al. 2016; A. T. P. Schauer et al. 2017;

S. Hegde & S. R. Furlanetto 2023). Inside minihalos, the gas fraction, density, and cold gas decrease, while the spin and rotational support of the halo increase (e.g., M. McQuinn & R. M. O'Leary 2012; S. Naoz et al. 2013; M. L. A. Richardson et al. 2013; Y. S. Chiou et al. 2018; A. T. P. Schauer et al. 2019; C. E. Williams et al. 2023). Streaming delays DM halo collapse, suppresses the cumulative halo mass function, generates gas-empty halos, and decreases the number of low-mass luminous galaxies (e.g., S. Naoz et al. 2012; J. Bovy & C. Dvorkin 2013; S. Asaba et al. 2016). Supermassive black hole formation can be enhanced, potential globular cluster progenitors can form, and some may be detectable by JWST (e.g., M. A. Latif et al. 2014a; T. L. Tanaka & M. Li 2014; S. Hirano et al. 2017; W. Lake et al. 2021, 2023a, 2023b, 2025; Y. Nakazato et al. 2022). The 21 cm signal before the formation of the first stars is enhanced/suppressed at different scales, and large-scale fluctuations are altered during reionization (e.g., M. McQuinn & R. M. O'Leary 2012; E. Visbal et al. 2012; Y. Ali-Haimoud et al. 2014; J. B. Muñoz 2019; C. Cain et al. 2020; H. Park et al. 2021). The BAO peak can be shifted in both Fourier space, configuration space, and when using the 21 cm signal as a probe (e.g., N. Dalal et al. 2010; J. Yoo et al. 2011; Z. Slepian & D. J. Eisenstein 2015; H. Long et al. 2022). The faint end of the UV luminosity function, as well as the star formation rate in dwarf galaxies, can also be enhanced at high redshift (e.g., W. Lake et al. 2024; C. E. Williams et al. 2024).

The stream velocity is also expected to inject turbulence into the gas of primordial halos that host Pop III stars (R. S. Klessen & S. C. O. Glover 2023). However, aside from T. H. Greif et al. (2011), which showed that the stream velocity enhances turbulence in the first collapsing minihalos in their simulations, no study has systematically examined how the stream velocity influences turbulence across a broad population of halos at the onset of Pop III star formation, nor explained what determines the resulting turbulence levels. An exception is M. A. Latif et al. (2014b), who found no significant impact of the stream velocity on turbulent energy, density, or radial velocities in halos at $z = 10$. However, this null result is not surprising, as the stream velocity has largely decayed by that redshift and is dynamically unimportant.

Turbulence is important and plays a key role in many astrophysical processes, including cosmic ray transport (e.g., A. Lazarian & A. Beresnyak 2006; A. Lazarian et al. 2023), regulation of the interstellar medium (e.g., D. Falceta-Gonçalves et al. 2014; K. W. Ho et al. 2023; K. H. Yuen et al. 2024), and star formation in local molecular clouds (e.g., M. R. Krumholz & C. F. McKee 2005; B. Burkhart 2018). Turbulence also plays a critical role in the formation of Pop III stars. Supersonic turbulence in primordial halos is generated during the virialization process and gravitational infall (e.g., J. H. Wise & T. Abel 2007; T. H. Greif et al. 2008; K.-J. Chen et al. 2025; M.-Y. Ho et al. 2025). This turbulence can lead to fragmentation of the cloud itself (e.g., K. Sugimura et al. 2023) or the protostellar disk, with the extent of fragmentation being influenced by both the magnitude of the turbulent energy and its mode—solenoidal versus compressive—and the rotational energy in the cloud (e.g., P. C. Clark et al. 2011; R. Riaz et al. 2018, 2023; K. M. J. Wollenberg et al. 2020). Turbulence can also amplify the magnetic fields by stretching and folding the field lines, which was shown to impact the initial mass function (IMF) of the Pop III stars (e.g., A. Stacy et al. 2022; K. E. Sadanari et al. 2024; P. Sharda & S. H. Menon 2025), and is the main source of angular momentum transport during the initial collapse (e.g., T. Abel et al. 2002; N. Yoshida et al. 2006; T. H. Greif et al. 2012). It can also enhance the abundances of coolants inside primordial halos (e.g., J. Prieto et al. 2012; C.-Y. Tang & K.-J. Chen 2024) and can seed the first quasars (M. A. Latif et al. 2022).

Turbulence in these primordial minihalos also resembles that observed in local molecular clouds and idealized simulations. J. Prieto et al. (2011) found that the velocity dispersion within these minihalos on scales of 100 pc is comparable to that in local molecular clouds. Additionally, the slope of the second-order structure function is marginally steeper than that observed in randomly driven supersonic turbulence (J. Prieto et al. 2011). The probability density function (PDF) of density in these halos exhibits a lognormal distribution, with parameters akin to those in supersonic turbulence simulations (C. Safranek-Shrader et al. 2012). In the local Universe, the density PDF is crucial for characterizing the star formation rate (e.g., B. Burkhart & P. Mocz 2019; S. M. Appel et al. 2023).

In this paper we study how the stream velocity modulates this turbulence by looking at its impact over a range of halos with different masses during the epoch of Pop III star formation. The paper is structured as follows. In Section 2, we describe the numerical setup of our simulations, including the implementation of the stream velocity. In Section 3, we show how the stream velocity changes the turbulent velocities in primordial halos, analyze its dependence on halo mass and redshift, and explain its physical origins. In Section 4, we interpret our findings in the context of previous work, explore their implications for Pop III star formation and accretion physics, and discuss possible observational consequences. In Section 5, we summarize our key results.

We assume a ΛCDM cosmology, with $\Omega_\Lambda = 0.73$, $\Omega_m = 0.27$, $\Omega_b = 0.044$, $\sigma_8 = 1.7$, and $h = 0.71$.

2. Numerical Methods

2.1. Initial Conditions

In order to correctly set the initial conditions (ICs) of our simulation, the perturbations of the cosmic microwave background (CMB) need to be self-consistently evolved with the streaming effect. Without this correction, the resulting simulation will overestimate the gas density amplitude in the power spectrum of select wavenumbers and can underestimate the distance the gas is shifted (S. Naoz & R. Narayan 2014; H. Park et al. 2020).

To ensure that the streaming effect is realized self-consistently, we generate separate transfer functions for DM and baryons by modifying the transfer functions from the CMBFAST code (U. Seljak & M. Zaldarriaga 1996). We add the streaming effect given in Equation (5) of D. Tseliakhovich et al. (2011) and add the scale-dependent temperature fluctuations δ_T discussed in S. Naoz & R. Barkana (2005). The resulting coupled perturbation equations can be written as (S. Naoz et al. 2013):

$$\ddot{\delta}_c + 2H\dot{\delta}_c - f_c \frac{2i}{a} \boldsymbol{v}_{bc} \cdot \boldsymbol{k} \dot{\delta}_c = \frac{3}{2} H_0^2 \frac{\Omega_m}{a^3} (f_b \delta_b + f_c \delta_c) + \left(\frac{\mathbf{v}_{bc} \cdot \boldsymbol{k}}{a} \right)^2 \delta_c, \quad (1)$$

$$\ddot{\delta}_{\rm b} + 2H\dot{\delta}_{\rm b} = \frac{3}{2}H_0^2\frac{\Omega_{\rm m}}{a^3}(f_{\rm b}\delta_{\rm b} + f_{\rm c}\delta_{\rm c}) - \frac{k^2}{a^2}\frac{k_{\rm B}\bar{T}}{\mu}(\delta_{\rm b} + \delta_{\rm T}), \quad (2)$$

and the evolution of $\delta_{\rm T}$ can be related to the evolution of the density by:

$$\dot{\delta}_{\rm T} = \frac{2}{3}\dot{\delta}_b + \frac{x_e}{t_\gamma a^4}\left[\frac{\bar{T}_\gamma}{\bar{T}}(\delta_{T_\gamma} + \delta_\gamma - \delta_{\rm T}) - \delta_\gamma\right]. \quad (3)$$

In these equations, f_b and f_c represent the cosmic baryon and cold DM fractions, while the variables δ_b, δ_c, δ_γ, δ_{T_γ}, and $\delta_{\rm T}$ denote the fluctuations in the baryon density, cold DM density, photon density, photon temperature, and baryon temperature, respectively. The mean photon and baryon temperatures are denoted by $\bar{T}_\gamma$ and $\bar{T}$. The quantity x_e represents the electron fraction out of the total number density of gas particles, with its time dependence described in S. Naoz & R. Narayan (2013). The Thomson scattering coupling time is defined as:

$$t_\gamma^{-1} \equiv \frac{8}{3}\bar{\rho}_\gamma^0\frac{\sigma_T c}{m_e} = 8.55 \times 10^{-13}\,{\rm yr}^{-1}, \quad (4)$$

and it governs the thermal coupling between baryons and the CMB. $\boldsymbol{v}_{\rm bc}$ is the average relative velocity between the baryons and DM in a given patch of space, and $\boldsymbol{k}$ is the comoving wavenumber vector. H is the Hubble parameter, H_0 is its present-day value, $\Omega_{\rm m}$ is the present-day matter density parameter, a is the scale factor, μ is the mean molecular weight, and $k_{\rm B}$ is the Boltzmann constant.

2.2. Cosmological Simulations

For our simulations, we use the quasi-Lagrangian code AREPO (R. Weinberger et al. 2020) that solves the equations of collisional and collisionless particles on a uniformly expanding, flat Friedmann–Lemaitre–Robertson–Walker spacetime. The mesh in AREPO moves with the flow and is constructed as a Voronoi tessellation of the simulation volume starting from a set of mesh-generating points.

The gas in the simulation cools using the primordial chemistry and cooling library Grackle (B. D. Smith et al. 2017; G. Chiaki & J. H. Wise 2019). Grackle tracks 49 nonequilibrium chemical reactions and their corresponding radiative cooling for the following 15 species: e^-, H, H^+, He, He^+, He^{++}, H^-, H_2, H_2^+, D, D^+, HD, HeH^+, D^-, and HD^+, with the most important lines being H_2 and HD cooling. The rate of radiative cooling of H_2 is computed for line transitions between 20 rotational and three vibrational levels, and for HD for three vibrational levels.

Our $(2\ {\rm Mpc})^3$ box contains 512^3 Voronoi gas cells with an initial mass of $m_{\rm gas} = 360\,M_\odot$ and 512^3 DM particles with an initial mass of $m_{\rm DM} = 1.9 \times 10^3\,M_\odot$. The simulation starts at $z = 200$ and terminates at $z = 20$. We run the simulation four times: one run does not include the stream velocity, and the other three runs have streaming strengths (with different ICs for streaming and no-streaming) of $v_{\rm bc} = 1\sigma_{\rm vbc}$, $v_{\rm bc} = 2\sigma_{\rm vbc}$, and $v_{\rm bc} = 3\sigma_{\rm vbc}$, where $\sigma_{\rm vbc}$ is the (scale-independent) rms fluctuation of the stream velocity. Since the size of our box is less than the coherence scale of the stream velocity, we can implement the stream velocity by giving each gas cell a uniform velocity boost in the $\hat{x}$-direction. For the main analysis, we focus on a rare patch of the Universe that has a stream velocity of $v_{\rm bc} = 2\sigma_{\rm vbc}$. This enables a clear isolation of the streaming effect, improving the diagnostic power of the analysis. It also allows for the full impact of streaming to be realized including the formation of gas structure outside the virial radius of DM halos (also known as Supersonically Induced Gas Objects or SIGOs; e.g., W. Lake et al. 2021) and is also similar to the estimated local value of $v_{\rm bc} = 1.75^{+0.13}_{-0.28}\sigma_{\rm vbc}$, based on simulating Milky Way–like galaxies with varying streaming velocities (B. Uysal & T. Hartwig 2023).[11] We set $\sigma_8 = 1.7$ to accelerate structure formation in our relatively small box. This has the effect of increasing the normalization of the halo abundances (S. Naoz et al. 2013) and the time objects form by a factor of $\sqrt{2}$ (H. Park et al. 2020) but does not otherwise affect the physics (e.g., N. Yoshida et al. 2007; A. Stacy et al. 2010, 2012; H. Susa et al. 2014; T. H. Greif et al. 2011). At initialization, we use a constant temperature of 422 K derived from linear theory, a softening length of $30\ h^{-1}$ pc, and set $\gamma = 5/3$. The simulations do not include magnetic fields or star formation with its accompanying feedback.

We use a standard friends-of-friends (FoF) algorithm to find halos and their associated gas cells (V. Springel et al. 2001), although this method has its limitations (see C. E. Williams et al. 2025). We first run the FoF on the DM particles using a linking length of 20% of the mean particle separation to identify DM halos. We then attach the gas cells within the halo in a secondary linking stage (C. Popa et al. 2016). We also compute the virial radius (assuming sphericity even though halos are triaxial (e.g., M. Vogelsberger et al. 2020)) of the halo as the radius enclosing a mean density of 200 times the critical density of the Universe. In our subsequent analysis, we only consider DM halos that contain at least 300 DM particles and 100 gas cells.

3. Results

3.1. Turbulence Inside Primordial Halos

To quantify turbulence within halos, we subtract the bulk, radial, and azimuthal rotational components from the velocities of the gas. The remaining random component of the velocity defines the turbulence:

$$v_{\rm turb} = \left(\frac{\sum_i m_i\,|\boldsymbol{v}_i - \boldsymbol{v}_{{\rm rot},i} - \boldsymbol{v}_{{\rm rad},i}|^2}{\sum_i m_i}\right)^{1/2}, \quad (5)$$

where the index i runs over all gas cells, m_i is the gas mass, $\boldsymbol{v}_i$ is the velocity relative to the center-of-mass velocity of the halo, $\boldsymbol{v}_{{\rm rad},i} = (\boldsymbol{v}_i \cdot \hat{\boldsymbol{r}}_i)\hat{\boldsymbol{r}}_i$ is the radial component of the velocity, and $\boldsymbol{v}_{{\rm rot},i} = \boldsymbol{r}_i \times \boldsymbol{\Omega}$ is the azimuthal rotational component of the velocity. $\boldsymbol{\Omega} = \boldsymbol{L}/I$ is the angular velocity of the gas, and $\boldsymbol{L}$ is the total angular momentum of the gas given by $\sum_i m_i(\boldsymbol{r}_i \times \boldsymbol{v}_i)$, where $I = \sum_i m_i|\boldsymbol{r}_i \times \hat{\boldsymbol{L}}|^2$ is the moment of inertia along the axis defined by the direction of $\boldsymbol{L}$ (see C. Safranek-Shrader et al. 2012). For each halo, we also compute rms, radial, and

[11] While we observe SIGOs in our simulations, we study their turbulent properties in future work since they only form in simulations with the stream velocity, and this work focuses on comparing turbulence inside halos with and without the stream velocity.

rotational velocities, given respectively as:

$$v_{\rm rms} = \left(\frac{\sum_i m_i |\boldsymbol{v}_i|^2}{\sum_i m_i} \right)^{1/2}, \quad (6)$$

$$v_{\rm rot} = \left(\frac{\sum_i m_i |\boldsymbol{v}_{{\rm rot},i}|^2}{\sum_i m_i} \right)^{1/2}, \quad (7)$$

and

$$v_{\rm rad} = \left(\frac{\sum_i m_i |\boldsymbol{v}_{{\rm rad},i}|^2}{\sum_i m_i} \right)^{1/2}. \quad (8)$$

In Figure 1, we show the mean turbulent, rms, rotational, and radial velocity as a function of total halo mass for both the streaming ($v_{\rm bc} = 2\sigma_{\rm vbc}$, blue curve) and no-streaming ($v_{\rm bc} = 0\sigma_{\rm vbc}$, red curve) runs. For this and other mass-binned plots, the streaming runs contain 955 halos with $M < 10^6\,M_\odot$, 1653 halos with $10^6\,M_\odot \leqslant M < 10^7\,M_\odot$, and 144 halos with $10^7\,M_\odot \leqslant M < 10^8\,M_\odot$, while the no-streaming run contains 1681, 2597, and 201 halos in these respective mass ranges. The data in these plots are binned in log-space and Gaussian smoothed for clarity. In the top panel we see that streaming enhances turbulent velocity in low-mass halos ($M \lesssim 10^6\,M_\odot$) while suppressing it in high-mass halos ($M \gtrsim 10^6\,M_\odot$). To confirm the robustness of this turnover, we perform a higher-resolution simulation (see Appendix) and find consistent results, including a clear turnover around $M \sim 10^6\,M_\odot$.

We also observe a strong correspondence between the rms (second panel from top) and turbulent velocity curves across both runs: the difference between the streaming and the no-streaming run is similar in magnitude and exhibits a turnover at approximately the same mass scale. This consistency is expected, as the turbulent velocity is computed from the rms velocity after subtracting coherent motions.

In the third panel of Figure 1, we show the rotational velocity curves. We see that streaming enhances rotational velocities across the entire mass range, consistent with prior studies that showed streaming increases halo spin parameters (e.g., Y. S. Chiou et al. 2018; M. Druschke et al. 2018; C. E. Williams et al. 2023). This effect likely arises from the coherent displacement of baryons relative to the halo center, which increases the net angular momentum of the system (M. Druschke et al. 2018).

To assess whether the turnover in the turbulent velocities reflects a statistically significant difference in the underlying distributions, we performed a two-sample Kolmogorov–Smirnov (KS) test on the turbulence values in the $v_{\rm bc} = 0\sigma_{\rm vbc}$ and $v_{\rm bc} = 2\sigma_{\rm vbc}$ runs, divided at the characteristic mass scale of $M = 10^6\,M_\odot$. For halos with $M < 10^6\,M_\odot$, we find a KS statistic of 0.35 with a p-value of $\sim 10^{-67}$, indicating a highly significant difference between the distributions. For halos with $M \geqslant 10^6\,M_\odot$, the KS statistic is 0.10 with a p-value of $\sim 10^{-9}$, demonstrating that the difference remains statistically significant, though less pronounced. These results confirm that the turnover in turbulence is not only visually apparent but also statistically robust.

The difference in average turbulent velocities between the streaming and no-streaming runs is most pronounced at high redshift and in low-mass halos, and generally decreases with time. In Figure 2, we show the percent difference in turbulent velocity as a function of total halo mass and redshift, computed

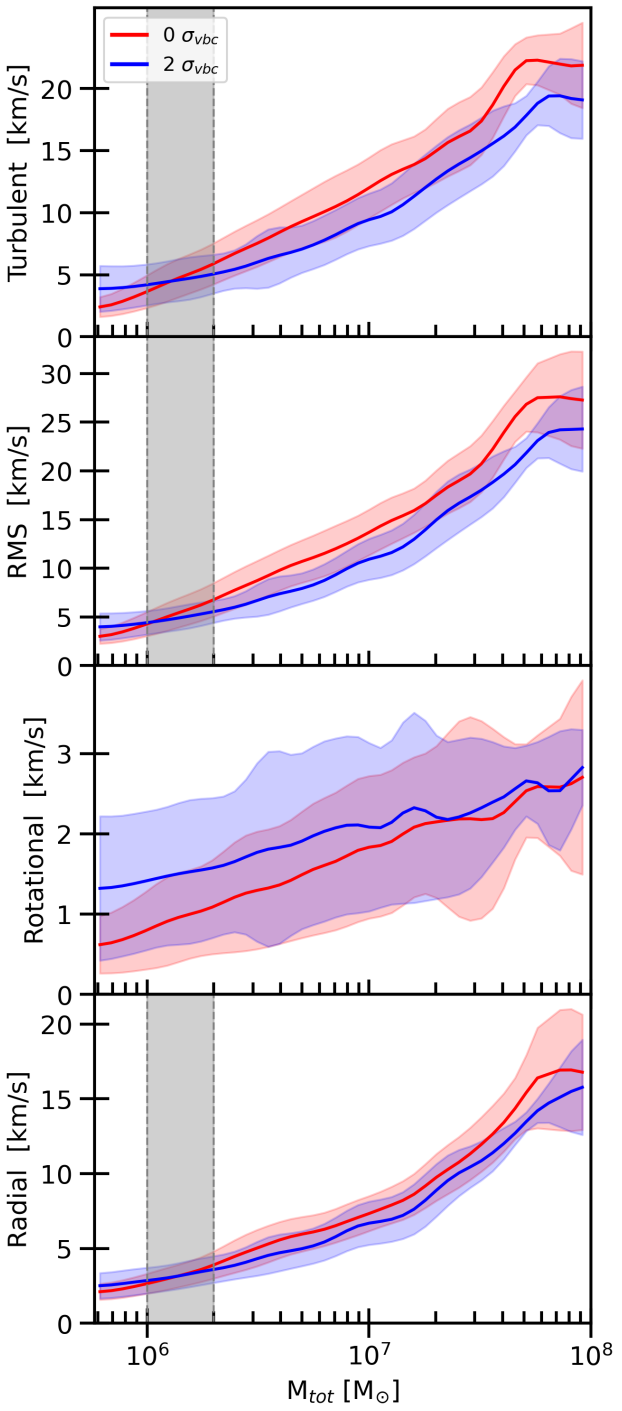

Figure 1. Comparison of kinematic properties of gas within halos in streaming ($v_{\rm bc} = 2\sigma_{\rm vbc}$, blue) and no-streaming ($v_{\rm bc} = 0\sigma_{\rm vbc}$, red), simulations at $z = 20$. Panels from top to bottom show turbulent velocity, rms velocity, radial velocity, and rotational velocity, each plotted against total halo mass (gas +DM). Shaded color bands indicate the 1σ scatter around the mean values. Streaming enhances turbulent and rms velocities in low-mass halos ($M \lesssim 10^6\,M_\odot$) but suppresses them in high-mass halos ($M \gtrsim 10^6\,M_\odot$), with a clear turnover around the characteristic mass scale marked by the gray shaded band. Rotational velocities are amplified across all halo masses in the presence of streaming, while radial velocities are higher in high-mass halos without streaming.

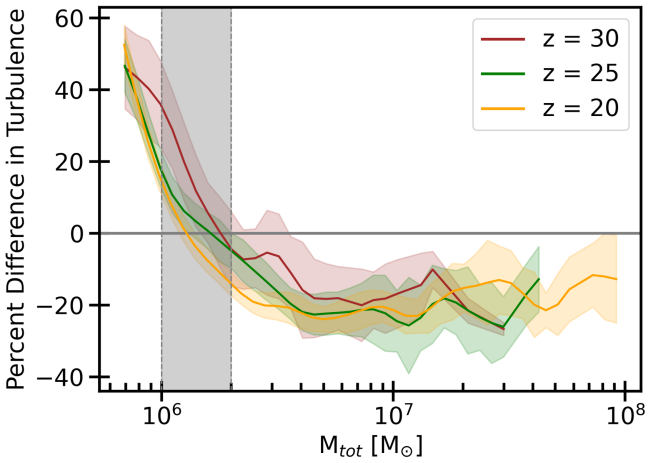

Figure 2. Percent difference in the turbulence with and without streaming at different redshifts. Shaded color bands indicate 1σ uncertainties, computed via standard error propagation of the ratio of means. The percent difference generally declines as a function of redshift as the stream velocity decays. The turnover at $M \sim 10^6\,M_\odot$ also shifts slightly toward higher masses at earlier times and is marked by the gray shaded band.

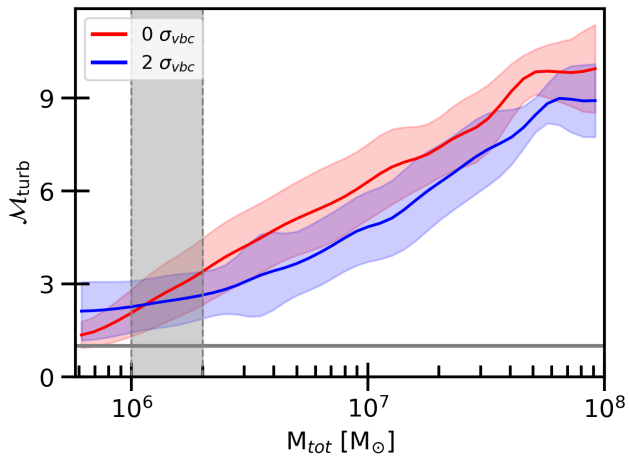

Figure 3. Turbulent Mach number as a function of total halo mass with and without streaming at $z = 20$. Shaded color bands indicate the 1σ scatter around the mean values. A clear turnover appears near $M \sim 10^6\,M_\odot$, marked by a gray band, mirroring the trend in the turbulent velocity (Figure 1). Horizontal gray line marks a Mach number of 1.

separately for each mass bin. The turnover remains near $M \sim 10^6\,M_\odot$ across all redshifts with a modest shift toward higher masses at earlier times. The percent difference is largest for low-mass halos, reaching factors of $\sim$1.5, and declines steeply with increasing mass. However, in higher-resolution runs, the percent difference appears to plateau at the lowest halo masses for the $v_{\rm bc} = 2\sigma_{\rm vbc}$ run, indicating a potential saturation in the streaming-induced boost (see Appendix). Future simulations with even higher resolution will be necessary to more precisely characterize the mass dependence of streaming-driven turbulence in halos with $M < 10^6 M_\odot$.

The turbulent Mach number is a key diagnostic of the compressibility and energetics of turbulence in the halo. Following T. H. Greif et al. (2012), we define it as:

$$\mathcal{M}_{\rm turb} = \frac{v_{\rm turb}}{\langle c_s \rangle}, \tag{9}$$

where $\langle c_s \rangle$ is the mass-weighted sound speed and $v_{\rm turb}$ is given by Equation (5). In Figure 3, we show the turbulent Mach number as a function of total halo mass. We see the clear bifurcation across $M \sim 10^6\,M_\odot$, analogous to the trend observed in the turbulent velocity. In low-mass halos ($M \lesssim 10^6\,M_\odot$), the turbulent Mach number is significantly enhanced in the streaming run, with boosts similar to those seen in the turbulent velocity. For halos of $M \sim 10^7\,M_\odot$ we find supersonic turbulence, with $\mathcal{M}_{\rm turb} \sim 6$ in the no-streaming run consistent with the values recently reported by K.-J. Chen et al. (2025) for similarly sized halos at comparable redshifts.

3.2. Possible Sources of the Turbulence

The enhancement of turbulence in low-mass halos (i.e., $M \lesssim 10^6\,M_\odot$) in the presence of a nonzero stream velocity is not surprising. At the time of recombination, the relative velocity between baryons and DM introduces coherent bulk motions into the gas. In our simulations, this is modeled as a uniform boost in the positive $\hat{x}$-direction. These bulk motions inject additional kinetic energy into the gas, which acts as an effective pressure that continuously suppresses density fluctuations on all scales. It also gets converted into radial and azimuthal motions along with turbulence inside low-mass DM halos through nonlinear interactions and the churning of the gas. These resulting velocities are dynamically important as their magnitudes are comparable to the sound speed in these halos.

The transition in turbulence near $M \sim 10^6\,M_\odot$ may result from a shift in the forces shaping the gas dynamics within these halos. In the absence of stellar feedback, the interplay between gravity and internal pressure, including thermal pressure and effective pressure from the stream velocity, determines the dynamics of the gas. As shown by D. Tseliakhovich et al. (2011), the filtering mass, a cumulative analog to the Jeans mass that accounts for the time-dependent suppression of baryonic fluctuations (e.g., N. Y. Gnedin 2000; S. Naoz & R. Barkana 2007), increases with an increased stream velocity. Interestingly, for $v_{\rm bc} = 2\sigma_{v_{\rm bc}}$ the filtering mass computed from linear theory is $1.07 \times 10^6\,M_\odot$ at $z = 20$, similar to the mass scale at which the turbulent velocity transitions from being enhanced to suppressed (see Table 1 in D. Tseliakhovich et al. 2011). However, the correspondence is suggestive rather than a one-to-one mapping, since for $v_{\rm bc} = 1\sigma_{v_{\rm bc}}$ and $v_{\rm bc} = 3\sigma_{v_{\rm bc}}$ we find the turnover in the turbulent velocity to be $M \sim 7 \times 10^5\,M_\odot$ and $M \sim 2 \times 10^6\,M_\odot$ (see Section 3.4) while the filtering mass is $1.85 \times 10^5\,M_\odot$ and $3.37 \times 10^6\,M_\odot$ respectively. Below the filtering mass, pressure forces, including those introduced by streaming, dominate and inhibit gas collapse, while above it, gravitational potential wells are sufficiently deep that pressure support becomes subdominant. This scale-dependent behavior is consistent with previous studies that showed the stream velocity has its greatest impact on low-mass halos by reducing the gas fraction, delaying baryonic collapse, and suppressing the formation of small-scale structure. (e.g., T. H. Greif et al. 2011; S. Naoz et al. 2012, 2013; C. Popa et al. 2016; Y. S. Chiou et al. 2018).

For halos with $M \gtrsim 10^6\,M_\odot$, the suppression of turbulence in the presence of streaming may at first seem counterintuitive. While the energy introduced by the stream velocity is expected to be less significant in high-mass halos, it is not immediately obvious why it would lead to a reduction in turbulence. A plausible explanation lies in an alternative mechanism of generating turbulence in primordial halos: accretion flows

(e.g., J. H. Wise & T. Abel 2007; T. H. Greif et al. 2008). As we will see, the stream velocity modifies the density field and accretion patterns, likely reducing the effectiveness of accretion-driven turbulence in high-mass halos.

To explore the possibility that the stream velocity suppresses accretion-driven turbulence in high-mass halos, we begin by analyzing the radial speed of incoming gas. In the bottom panel of Figure 1, we show the mass-weighted rms radial velocity magnitude of gas within halos as a function of total mass. For halos $M \gtrsim 10^6\,M_\odot$ we see a slight increase in the kinetic energy associated with radial motions without streaming. The gas inside the halos is also denser without streaming (e.g., R. M. O'Leary & M. McQuinn 2012; M. L. A. Richardson et al. 2013). Taken together, this suggests that the energy of accretion flows will be higher in high-mass halos without streaming. This inflowing accreting gas can generate turbulence through shear flows, instabilities, or the thermalization of kinetic energy via shocks. We explore the latter phenomenon in Section 3.5.

One possible explanation for the elevated radial velocities observed in more massive no-streaming halos is their deeper gravitational potential wells (e.g., C. E. Williams et al. 2025). We can compute the total gravitational potential energy of each halo by summing three contributions: gas–gas self-interaction, DM–DM self-interaction, and gas–DM cross-interaction. These quantities are calculated using all gas cells and DM particles associated with each halo. The total potential energy is given by:

$$U_{\rm total} = U_{\rm gas\text{-}gas} + U_{\rm dm\text{-}dm} + U_{\rm gas\text{-}dm}\ . \tag{10}$$

Each term is calculated via pairwise summation over cell and particle pairs:

$$\begin{aligned} U_{\rm gas\text{-}gas} &= -\frac{1}{2}G\sum_{i\neq j}^{N_{\rm gas}}\frac{m_i m_j}{|\boldsymbol{r}_i-\boldsymbol{r}_j|}\ ,\\ U_{\rm dm\text{-}dm} &= -\frac{1}{2}G\sum_{i\neq j}^{N_{\rm dm}}\frac{m_i m_j}{|\boldsymbol{r}_i-\boldsymbol{r}_j|}\ ,\\ U_{\rm gas\text{-}dm} &= -G\sum_{i=1}^{N_{\rm gas}}\sum_{j=1}^{N_{\rm dm}}\frac{m_i m_j}{|\boldsymbol{r}_i-\boldsymbol{r}_j|}\ . \end{aligned} \tag{11}$$

where m_i and $\boldsymbol{r}_i$ denote the mass and position of particle i, and G is the gravitational constant in units of kiloparsecs $(\mathrm{km/s})^2 M_\odot^{-1}$. In Figure 4, we plot the total gravitational potential energy as a function of halo mass. We find that halos with no-streaming exhibit deeper potential wells compared to their streaming counterparts. This is expected as the stream velocity makes it harder for potential wells to form by adding an effective anisotropic pressure to the gas. This is the same underlying physics that causes a suppression of the gas density (in halos of all sizes) and the decrease in the number of DM halos. For a fixed halo mass, a deeper gravitational potential would lead to greater radial energies in accreting flows. These larger radial velocities would amplify turbulence and could help explain the trends seen in Figures 1 and 2.

Mergers are also known to generate turbulence inside primordial halos (e.g., J. H. Wise & T. Abel 2007; J. Prieto et al. 2012; S. Bovino et al. 2014). They also raise the temperatures of the gas (e.g., N. Yoshida et al. 2003), which would increase the accretion rate of the halo (e.g., S. Hirano et al. 2015). Although the impact of the stream velocity on mergers has not yet been studied, it is reasonable to expect a

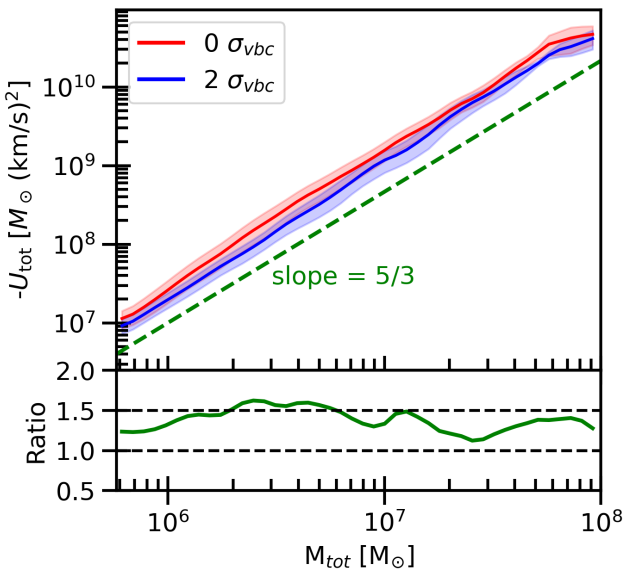

Figure 4. Gravitational potential energy of halos as a function of total mass (gas + DM) at $z = 20$ with and without streaming. The top panel shows the halo's gravitational potential energy, computed from gas–gas, DM–DM, and gas–DM interactions for all gas cells and dark matter particles within each halo. The green dashed line shows the expected scaling of slope 5/3 for virialized halos. Shaded color bands indicate the 1σ scatter around the mean values. The bottom panel shows the ratio of the two curves. No-streaming halos exhibit systematically higher potential energies across the full mass range.

suppression. As mentioned in Section 3.1, streaming reduces the number of halos across all mass scales, with the most pronounced effect in the low-mass regime, where the abundance is diminished by roughly a factor of 1.8 for halos $M \leqslant 10^6\,M_\odot$. We thus expect fewer mergers, especially minor mergers, in the presence of the stream velocity, since the number of mergers should be positively correlated with the number of halos. The stream velocity also adds an effective anisotropic pressure to the gas, which can also act to suppress mergers on all scales. This reduction in mergers may contribute to the observed suppression of turbulence in high-mass halos when streaming is present.

To qualitatively explore this possibility, we look at the environments of typical halos above and below the turnover of $M \sim 10^6\,M_\odot$. In the top panel of Figure 5 we show three typical halos with $M < 10^6\,M_\odot$ for streaming and no-streaming in a 1 kpc cutout centered on the center of mass of the selected halo, and in the bottom panel, we show three typical halos with $M = 10^6$–$10^7\,M_\odot$ at $z = 20$. For both streaming and no-streaming, we see that halos with $M < 10^6\,M_\odot$ generally exist in isolation, residing along wisps of cosmic filaments. On the other hand, for halos with $M = 10^6$–$10^7\,M_\odot$ we see that the no-streaming halos now exist in a more complex environment, with more nearby structures and multiple knots of cosmic filaments. The streaming halos, on the other hand, still form in less crowded environments, with fewer structures and fewer intersected cosmic filaments. Thus, it is more likely that mergers, the likelihood of which increases with halo mass, are preferentially increasing the turbulence for high-mass halos in the no-streaming run.

3.3. The Intergalactic Medium

We next look at the properties of the intergalactic medium (IGM) at $z = 20$ to further explore whether the enhancement in turbulence in the no-streaming high-mass

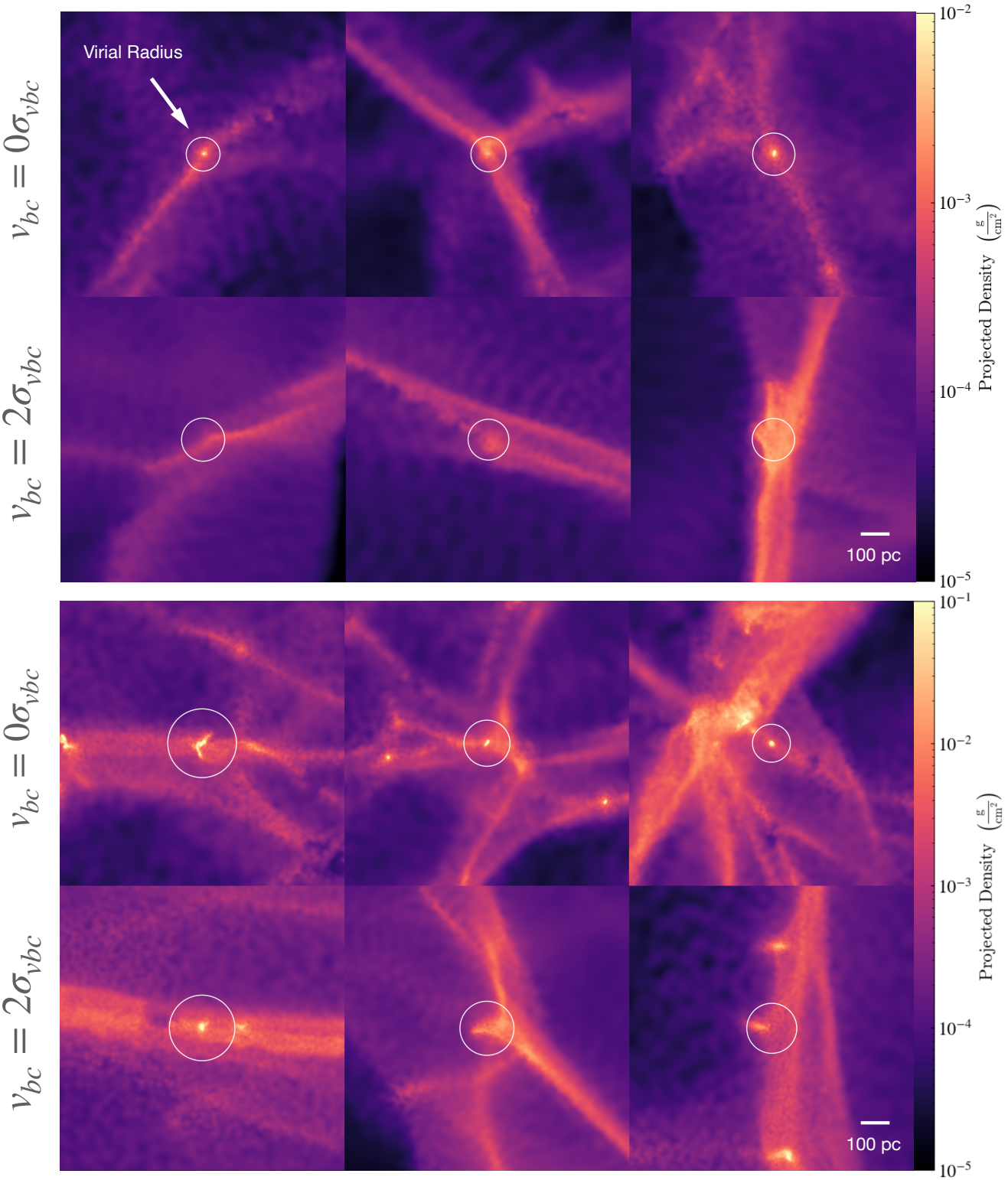

Figure 5. Projected gas density surrounding representative halos from two mass bins in simulations with streaming (bottom rows in each pair) and without streaming (top rows in each pair) at $z = 20$. Each panel shows a 1 kpc (physical) cutout centered on the halo's center of mass. The top pair depicts halos with $M < 10^6\,M_\odot$, while the bottom pair depicts halos in the range $M = 10^6$–$10^7\,M_\odot$. White circles denote the virial radius of each halo. Low-mass halos appear similarly isolated in both streaming and no-streaming runs and are embedded along thin filaments. In contrast, higher-mass halos without streaming reside in denser environments with more frequent filamentary intersections and nearby structures, conditions favorable for mergers. This visual difference suggests that streaming may suppress merger-driven turbulence in high-mass halos by reducing the abundance of dense nearby structures.

halos is related to the turbulence generated during accretion. In Figure 6, we show the probability density functions (PDFs) of gas velocity (left panel) and number density (right panel) for all gas not inside DM halos, as defined in Section 2.2. The bottom panels in each figure show the corresponding ratios between the curves.

The velocity PDFs indicate that by at least this epoch, the stream velocity's kinematic imprint is no longer prominent in

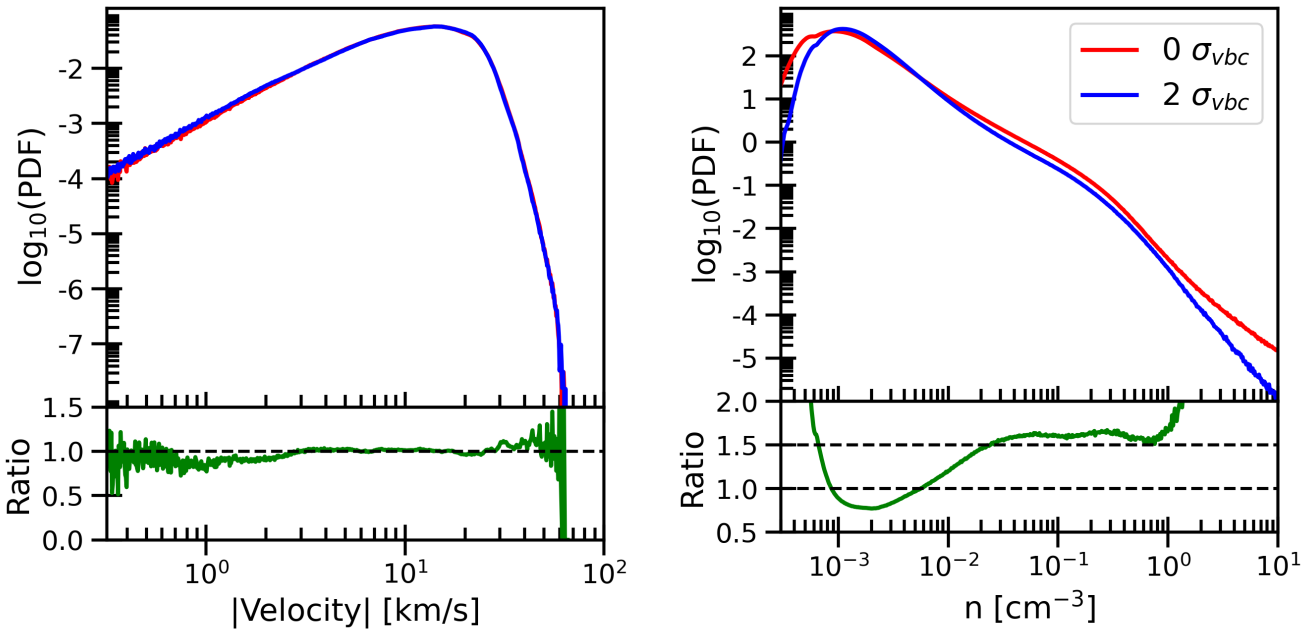

Figure 6. Probability density functions (PDFs) of gas velocity (left) and number density (right) in the intergalactic medium (IGM) at $z = 20$ with and without streaming. The IGM is defined as all gas not inside halos as identified by the FoF. Bottom subpanels show the ratio of the PDFs in each run. While the velocity distributions are nearly identical, indicating that the kinematic imprint of streaming has largely dissipated by this epoch, the number density distribution reveals a suppression of dense filamentary gas ($n \gtrsim 10^{-1}\,\mathrm{cm}^{-3}$) in the streaming run. This difference, integrated over cosmic time, contributes to reduced kinetic energy and turbulence in gas accreting onto halos in the presence of streaming.

the IGM. The bulk of the gas exhibits velocities well in excess of the decayed streaming value, and both simulations yield nearly identical velocity distributions for gas not inside halos. This suggests that the residual effect of the stream velocity on the velocities in the IGM is negligible, consistent with what was shown earlier that the stream velocity's influence persists primarily in halos with $M \lesssim 10^6\,M_\odot$.

The number density PDF reveals a more pronounced difference. For the most diffuse gas ($n \sim 10^{-3}\,\mathrm{cm}^{-3}$), which constitutes the majority of the IGM by volume, the peak of the density distribution is similar in both runs. In the cosmic filaments, however, which have typical densities $n \gtrsim 10^{-1}\,\mathrm{cm}^{-3}$, streaming suppresses the gas densities. This suppression is a cumulative effect over cosmic time and is consistent with the diffuse gas observed in halos. When this denser gas accretes into the halos, it will have higher kinetic energy and will therefore generate more turbulence during accretion. It will also thermalize more of its energy, something we explore in the next section. Despite the suppression of gas densities with streaming, however, mass conservation is maintained, as the displaced gas is redistributed into lower-density regions of the IGM.

3.4. Turbulence with Varying Stream Velocities

Having determined the possible cause of the turnover in the turbulent velocity for $v_{\rm bc} = 2\sigma_{\rm vbc}$ we now show how the turnover changes with varying the stream velocity. Since the cause of the turnover is expected to be the same for all streaming strengths (injection of energy in low-mass halos and suppression of accretion-driven turbulence and merger-driven turbulence in high-mass halos), in this section we highlight the percent difference in the turbulent velocity as a function of streaming strength at $z = 20$.

The turnover in turbulent velocity persists for both $v_{\rm bc} = 1\sigma_{\rm vbc}$ and $v_{\rm bc} = 3\sigma_{\rm vbc}$ and increases with increasing streaming strength. In Figure 7, we show the percent difference as a function of total halo mass for all three runs at $z = 20$. For each case, we compute the percent difference in turbulent velocity relative to the no-streaming ($v_{\rm bc} = 0\sigma_{\rm vbc}$) simulation, separately in each mass bin. The $v_{\rm bc} = 3\sigma_{\rm vbc}$ run exhibits both a stronger enhancement in turbulent velocity in low-mass halos and a shift of the turnover mass to higher values. In contrast, the $v_{\rm bc} = 1\sigma_{\rm vbc}$ run shows a more modest enhancement, with the turnover beginning around $M \sim 7 \times 10^5\,M_\odot$. For high-mass halos, we observe the expected inverse trend: turbulent velocity is suppressed relative to the no-streaming case, and this suppression becomes weaker with decreasing $v_{\rm bc}$. For all three runs, the relationship between streaming and turbulent velocity is as expected, illustrating the common cause of all three curves.

3.5. Thermalization of Accretion Shocks

As discussed in Section 3.4, the enhanced turbulent velocities in high-mass halos without streaming may be linked to accretion-driven turbulence. To further explore this possibility, we analyze the thermalization of accretion-driven shocks using the shock finder developed by K. Schaal & V. Springel (2015), K. Schaal et al. (2016). The shock finder loops over all gas cells, identifies those that have been shocked[12] and computes the energy dissipation rate along with the Mach number for each shocked cell. The energy dissipation rate of the shock, the quantity of interest, is computed by dividing the thermal

[12] Here we summarize the shock finder principles: it first identifies a shock zone comprising cells that satisfy three criteria: (i) the flow is compressive, $\nabla \cdot \boldsymbol{v} < 0$; (ii) the temperature and density gradients are aligned, $\nabla T \cdot \nabla \rho > 0$; and (iii) the logarithmic jumps in temperature and pressure each exceed a threshold corresponding to a minimum Mach number of 1.3, to avoid spurious shocks. From each shock zone cell, rays are cast along the direction of increasing temperature (i.e., toward the postshock region) and then reversed toward the preshock region. The cell with the most negative velocity divergence (i.e., maximum compression) along this path is tagged as part of the shock surface. These shock surface cells are the ones considered shocked; see Figure 1 of K. Schaal & V. Springel (2015) for an illustration.

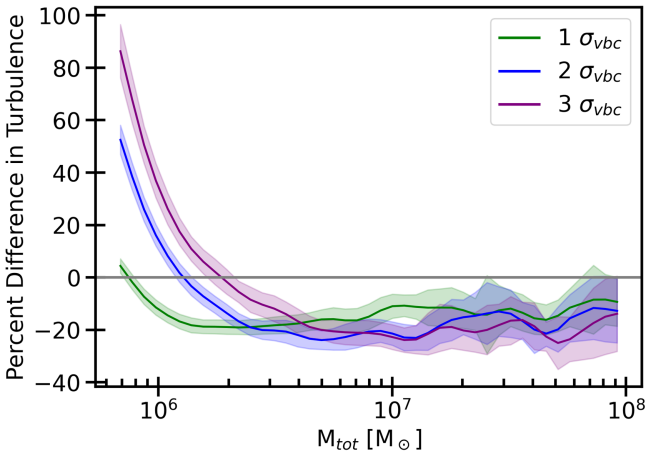

Figure 7. Percent difference in turbulent velocity between streaming ($v_{bc} = 1\sigma_{vbc}$, $v_{bc} = 2\sigma_{vbc}$, $v_{bc} = 3\sigma_{vbc}$) and no-streaming ($v_{bc} = 0\sigma_{vbc}$) simulations as a function of total halo mass. Shaded color bands indicate the 1σ uncertainties, computed via standard error propagation of the ratio of means. The percent difference is computed separately in each mass bin. The enhancement of turbulence grows with increasing streaming for low-mass halos ($M \lesssim 10^6\,M_\odot$), while turbulence is suppressed at higher masses across all streaming strengths.

energy flux by the surface of the shocked Voronoi cell. The thermal energy flux is given by:

$$f_{\rm th} = \delta(\mathcal{M}) f_\Phi, \tag{12}$$

where f_Φ is the incoming kinetic energy and $\delta(\mathcal{M})$ is the thermalization efficiency. The incoming kinetic energy is given by:

$$f_\Phi = \frac{1}{2}\rho_1 (c_1 \mathcal{M})^3, \tag{13}$$

and the thermalization efficiency is given by (H. Kang et al. 2007):

$$\delta(\mathcal{M}) = \frac{2}{\gamma(\gamma-1)\mathcal{M}^2 R}\left[\frac{2\gamma\mathcal{M}^2 - (\gamma-1)}{(\gamma+1)} - R^\gamma\right], \tag{14}$$

where R is the density jump given by:

$$R \equiv \frac{\rho_2}{\rho_1} = \frac{(\gamma+1)\mathcal{M}^2}{(\gamma-1)\mathcal{M}^2 + 2}. \tag{15}$$

In Figure 8 we show the distribution of shocks for a no-streaming halo of mass $M \simeq 10^7\,M_\odot$. In the top panel, we show the shocked gas cells in blue along with the virial radius of the halo represented by a green circle overlaid with normalized velocity vectors, colored red for those outside the virial radius and yellow for those inside. In this particular halo, shocked gas is found both inside and outside the virial radius. The bottom panel shows the corresponding temperature distribution of the gas, with shocked cells marked by black circles. We find that some of the shocked gas reaches temperatures comparable to the virial temperature of the halo, which we compute as:

$$T_{\rm vir} = \frac{\mu m_p}{2k_{\rm B}}\frac{GM_{\rm vir}}{R_{\rm vir}}, \tag{16}$$

where $\mu = 1.22$ is the mean molecular weight for neutral primordial gas, m_p is the proton mass, $k_{\rm B}$ is the Boltzmann constant, and G is the gravitational constant. For this halo, we find $T_{\rm vir} = 1.12 \times 10^4$ K.

The measured energy dissipation from shocked gas provides further support that streaming may suppress accretion-driven turbulence in high-mass halos. In Figure 9 we show the average energy dissipation rate of shocked gas inside halos as a function of halo mass. We see that for halos with $M \gtrsim 2 \times 10^6\,M_\odot$, no-streaming halos exhibit systematically higher energy dissipation. When this energy is thermalized in shocks, some of it can transform into nonthermal motions through postshock Richtmyer–Meshkov and Kelvin–Helmholtz instabilities, which will stir the gas and generate turbulence. Thus, no-streaming halos, which have a higher energy dissipation rate, will also have higher turbulence associated with these shocks. In Figure 9 we also see that the energy dissipation rate turns over at around the same mass scale as the turbulence (i.e., $M \sim 10^6\,M_\odot$), further suggesting a causal link.

The enhanced energy dissipation observed in high-mass halos without streaming can be partly attributed to the denser infalling intergalactic gas. As discussed in Section 3.3 and shown in Figure 6, filamentary structures in the no-streaming case exhibit systematically higher densities. When this denser material accretes onto halos, it carries greater kinetic energy, leading to an elevated thermal energy flux upon shocking as described by Equation (12). The thermalization efficiency, however, also depends on the Mach number, which, though saturating to a max value of 0.55 for $\gamma = 5/3$ when $\mathcal{M} \approx 10$, will also play a role in determining the energy dissipation rate. Combined with the higher radial velocities shown in Figure 1, these denser inflows likely contribute to stronger shock heating and enhanced accretion-driven turbulence in high-mass halos in the no-streaming run. We note that although our increased σ_8 accelerates structure formation and leads to a denser cosmic environment at fixed redshift, the relative trends remain robust for any given choice of σ_8, as both simulations experience the same shift in collapse timing.

4. Discussion

The enhancement of turbulence and rotational velocities in low-mass halos in the presence of streaming is consistent with prior works. T. H. Greif et al. (2011) found that for a $v_{bc} = 1\sigma_{vbc}$ turbulence is increased in minihalos ($M \lesssim 10^6\,M_\odot$) during runaway collapse, defined by central densities reaching $n_{\rm H} = 10^9\,{\rm cm}^{-3}$. Although halos in our cosmological simulation do not reach these number densities, we still observe enhanced turbulence for halos in a similar mass range. This suggests that turbulent kinetic energy present at the halo scale cascades to smaller scales, a process also known to occur in local molecular clouds (e.g., R. B. Larson 1981). The higher rotational velocities we find in the streaming runs are likewise consistent with the elevated spin parameters generated by streaming (e.g., Y. S. Chiou et al. 2018; M. Druschke et al. 2018; C. E. Williams et al. 2023).

The stream velocity may also influence the Pop III IMF in a halo mass-dependent manner. If star formation first occurs in halos with $M \lesssim 10^6\,M_\odot$, then our results and those of T. H. Greif et al. (2011) suggest that streaming-induced turbulence is enhanced on both large and small scales. This enhanced turbulence in low-mass halos, which may be amplified during gravitational contraction (e.g., S. Higashi et al. 2021), may increase fragmentation and may be contributing to the increased star formation rates found in low-mass objects in W. Lake et al. (2024).

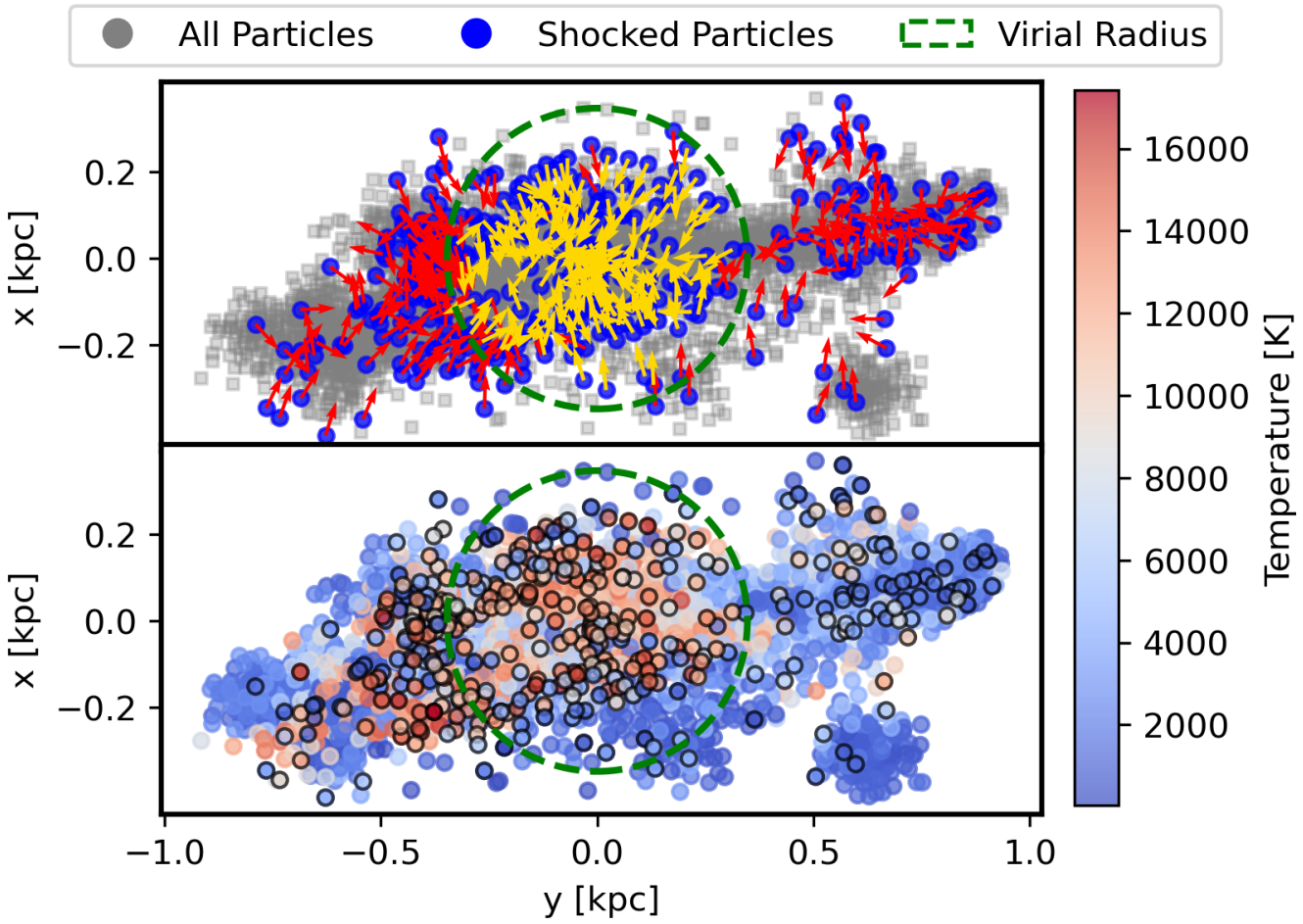

Figure 8. Shocked gas in an illustrative halo of mass $M \simeq 10^7\,M_\odot$ at $z = 20$. Top panel: All gas within the halo is shown in gray, while shocked gas is overplotted in blue. Red arrows indicate normalized velocity vectors of shocked gas outside the virial radius of the halo, and yellow arrows indicate those inside. The dashed green circle marks the virial radius. We see that the shocked gas predominantly traces radially oriented accretion shocks. Bottom panel: Gas temperature distribution, where shocked gas is outlined in black. Shocked gas reaches temperatures near the virial temperature, consistent with strong thermalization during accretion.

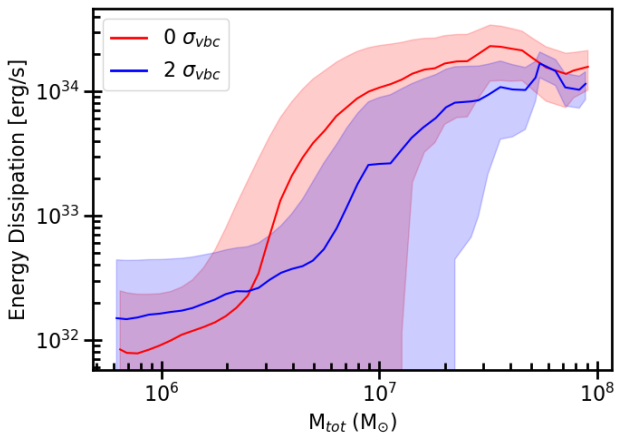

Figure 9. Average energy dissipation rate from shocked gas as a function of total halo mass at $z = 20$. Shaded color bands indicate the 1σ scatter around the mean values. At high-mass halos ($M \gtrsim 10^6\,M_\odot$), no-streaming halos exhibit higher dissipation rates, consistent with enhanced energy in accretion flows.

Streaming is also known to delay the onset of Pop III star formation and to raise the halo mass threshold at which collapse occurs (e.g., M. Kulkarni et al. 2021; U. Maio et al. 2011; A. Stacy et al. 2011; S. Hirano et al. 2018). These more massive halos typically collapse more rapidly and tend to form a greater number and more massive stars (e.g., B. Liu et al. 2024; S. Hirano 2025). If star formation primarily occurs in halos with $M \gtrsim 10^6\,M_\odot$, as suggested by the critical halo mass threshold, $M_{\rm crit}$ (e.g., M. Kulkarni et al. 2021; A. T. P. Schauer et al. 2021; S. Hegde & S. R. Furlanetto 2023; O. Nebrin et al. 2023), then our results indicate that streaming suppresses turbulence relative to no-streaming halos of similar halo mass at the same redshift (Figure 1). At fixed halo mass, the differing levels of turbulence may lead to variations in the IMF, as turbulence is known to promote fragmentation both at the cloud scale (K. Sugimura et al. 2023) and within protostellar disks (e.g., P. C. Clark et al. 2008; K. M. J. Wollenberg et al. 2020; R. Riaz et al. 2023). This, of course, does not account for feedback from the differing star formation histories between streaming and no streaming. This critical mass threshold can also be modulated by additional backgrounds, increasing in the presence of a uniform Lyman–Werner field (e.g., M. Kulkarni et al. 2021; A. T. P. Schauer et al. 2021), or decreasing with a uniform X-ray background (e.g., J. A. Hummel et al. 2015; H. Park et al. 2021) or under the influence of cosmic rays (J. A. Hummel et al. 2016).

Streaming enhancement of rotational motions and halo spin could also impact the number and masses of protostars. Enhanced rotational motions in collapsing clouds generally inhibit protostellar disk fragmentation and reduce the mass accretion onto individual protostars (e.g., S. Hirano et al. 2014; R. Riaz et al. 2018; K. M. J. Wollenberg et al. 2020; O. Jaura et al. 2022). Although the scales we study are larger than those examined in core-scale simulations, conservation of angular momentum suggests that enhanced large-scale rotation may cascade inward. The elevated spin parameters seen in streaming runs may even impact the orbital structure of protostars (K. Sugimura et al. 2023). How this enhancement in rotational motions couples with the turbulent velocities to impact the IMF will require further high-resolution simulations.

The accretion shocks identified in our simulations are similar to those reported in recent high-resolution studies of primordial halos. M. Kiyuna et al. (2023) showed that accreting gas onto halos of mass $5.0 \times 10^6\,M_\odot$ experiences shocks at around the virial radius at $z = 20$. Similar results were also found in R. Fernandez et al. (2014) & J. H. Wise & T. Abel (2007). Halos in our simulation also exhibit shock-heated gas near the virial radius, with some halos showing shocked gas extending into the halo interior, as depicted in Figure 8.

The classical framework for describing gas accretion distinguishes between hot-mode and cold-mode accretion. In this paradigm, low-mass halos accrete gas via cold streams along filaments that penetrate the halo without shock heating to the virial temperature, while in more massive halos, gas undergoes spherical accretion shocks and is heated to the virial temperature (Y. Birnboim & A. Dekel 2003; D. Kereš et al. 2005). The recent works of M. Kiyuna et al. (2023) and R. Fernandez et al. (2014) have added subtleties to this paradigm in the high-redshift Universe. The former by showing that the gas temperature along accretion columns is $T \sim 10^4$ K, and the latter by not observing cold accretion in their halos even though they nominally satisfy the criterion of Y. Birnboim & A. Dekel (2003). While in this study we do not closely follow the thermal history of individual gas streams to determine when and how cold-mode accretion occurs, we do find that at least some of the accreting gas is shock-heated near and inside the virial radius in low-mass halos.

The differences in energy dissipation rates of shocks induced by the stream velocity may lead to observable consequences. R. M. O'Leary & M. McQuinn (2012) found bow shocks surrounding DM halos in the presence of streaming, and concluded that these shocks, as well as structure formation shocks, with or without streaming, would not erase a strong 21 cm absorption signal. However, they noted the caveat that the fraction of kinetic energy thermalized in these shocks remained uncertain (M. McQuinn & R. M. O'Leary 2012). In our simulations, we find shocked gas reaching temperatures of 10^4 K, consistent with those reported by R. Fernandez et al. (2014) and M. Kiyuna et al. (2023). These shocks may accelerate electrons, leading to inverse Compton (IC) emission spanning radio to soft X-ray frequencies, potentially detectable with upcoming instruments (S. R. Furlanetto & A. Loeb 2004). A study into whether the differences in shock energy dissipation observed in our simulations could produce an observable signature of the stream velocity is left for future work.

5. Conclusion

In this paper, we sought to explain, for the first time, how the stream velocity impacts turbulence across a range of halo masses in the high-redshift Universe. In addition to previously recognized drivers of turbulence in primordial halos, such as accretion flows and halo mergers, we find that the stream velocity itself can be a significant source of turbulence in low-mass halos. Our primary results can be summarized as follows:

1. We identify a mass threshold of $M \sim 10^6\,M_\odot$ that separates two distinct regimes. In halos below this threshold, the stream velocity enhances turbulence, whereas in halos above the threshold, it suppresses it (Section 3.1). The enhancement for low-mass halos is likely sourced by the increased kinetic energy introduced by the stream velocity, while the suppression in high-mass halos likely results from weaker accretion-driven turbulence in the presence of the stream velocity.
2. At $z = 20$, the velocity distribution of intergalactic gas is nearly identical in simulations with and without streaming, indicating that the kinematic imprint of the stream velocity has largely dissipated from the IGM. However, the density PDF shows that filamentary structures feeding DM halos remain systematically denser in the no-streaming run (Section 3.3). Additionally, halos without streaming exhibit deeper gravitational potential wells across all masses and higher radial velocities in high-mass halos. Together, these trends imply that accretion flows onto high-mass halos are more energetic in the absence of streaming.
3. The average energy dissipation rate from shocks exhibits a similar mass-dependent trend as the turbulence, with a turnover near $M \sim 2 \times 10^6\,M_\odot$. At higher masses, halos without streaming show greater shock dissipation rates than their streaming counterparts (Section 3.5), consistent with the enhanced turbulence seen in this regime. This correlation supports the argument that more energetic accretion flows, facilitated by deeper potential wells and denser filaments, contribute to stronger shock heating and potentially to greater turbulence in high-mass halos without streaming.

The stream velocity thus influences gas dynamics in two opposing ways: it enhances turbulence in low-mass halos by introducing additional kinetic energy into the gas, and suppresses turbulence in high-mass halos by lowering their potentials and reducing gas density both inside and outside halos. Which of these effects dominates depends on halo mass, with a transition occurring near $M \sim 10^6\,M_\odot$. This mass-dependent behavior suggests that the star formation at a fixed DM halo mass may differ in the presence of the stream velocity and could be relevant for future high-resolution, full-physics simulations seeking to model the first stars with the stream velocity.

Acknowledgments

A.C. would like to thank K. H. Yuen for inspiring discussions. A.C., C.E.W., W.L., B.B., S.N., F.M., and M.V. thank the support of NASA grant Nos. 80NSSC20K0500 (19-ATP19-0020) and 80NSSC24K0773 (23- ATP23-0149). B.B. acknowledges support from NSF grant AST-2009679. This research was also supported in part by the National Science Foundation under grant No. NSF PHY-1748958. B.B. is grateful for generous support from the David and Lucile Packard Foundation, the Alfred P. Sloan Foundation, and the Flatiron Institute, which is funded by the Simons Foundation.

C.E.W. acknowledges the support of the National Science Foundation Graduate Research Fellowship, the University of California, Los Angeles (UCLA), the UCLA Center for Diverse Leadership in Science Fellowship, and the UCLA Mani L. Bhaumik Institute for Theoretical Physics Fellowship. This material is based upon work supported by the National Science Foundation Graduate Research Fellowship Program under grant No. DGE-2034835. Any opinions, findings, conclusions, or recommendations expressed in this material are those of the author(s) and do not necessarily reflect the views of the National Science Foundation. S.N. thanks Howard and Astrid Preston for their generous support. The simulations and computations in this paper were carried out on the Rusty supercomputer at the Flatiron Institute.

Software: `AREPO` (R. Weinberger et al. 2020), matplotlib (J. D. Hunter 2007), numpy (C. R. Harris et al. 2020), scipy (P. Virtanen et al. 2020), and `yt` (M. J. Turk et al. 2011).

Appendix
Resolution Study

To assess the impact of resolution on our velocity curves, we repeat the analysis using a higher-resolution setup: a $(2.5\ \mathrm{Mpc})^3$ box containing 768^3 Voronoi gas cells (with initial gas mass $m_{\rm gas} = 200\,M_\odot$) and 768^3 dark matter particles (with initial mass $m_{\rm DM} = 1.1 \times 10^3\,M_\odot$). In Figure 10, we show the rms and turbulent velocities from this simulation. The characteristic turnover in turbulent velocity between the streaming and no-streaming runs persists at $M \sim 10^6\,M_\odot$. Additionally, the difference in turbulence appears to begin saturating at the lowest resolved halo masses. Even higher-resolution simulations capable of probing lower-mass halos will be necessary to determine whether this trend continues.

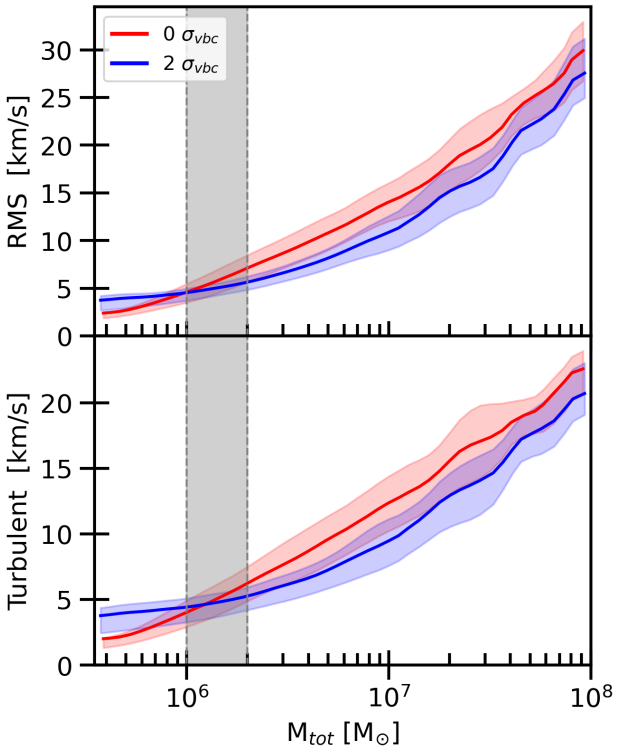

Figure 10. RMS and turbulent velocities as a function of halo mass in the higher-resolution run. Shaded color bands indicate the 1σ scatter around the mean values. The turnover in turbulence remains at $M \sim 10^6\,M_\odot$, marked by the gray shaded band, while the difference between streaming and no-streaming begins to saturate for the lowest-mass halos.

ORCID iDs

Avi Chen https://orcid.org/0000-0002-8859-7790
William Lake https://orcid.org/0000-0002-4227-7919
Claire E. Williams https://orcid.org/0000-0003-2369-2911
Blakesley Burkhart https://orcid.org/0000-0001-5817-5944
Smadar Naoz https://orcid.org/0000-0002-9802-9279
Shyam H. Menon https://orcid.org/0000-0001-5944-291X
Federico Marinacci https://orcid.org/0000-0003-3816-7028
Mark Vogelsberger https://orcid.org/0000-0001-8593-7692
Naoki Yoshida https://orcid.org/0000-0001-7925-238X

References

Abel, T., Bryan, G. L., & Norman, M. L. 2002, Sci, 295, 93
Ali-Haimoud, Y., Meerburg, P. D., & Yuan, S. 2014, PhRvD, 89, 083506
Appel, S. M., Burkhart, B., Semenov, V. A., et al. 2023, ApJ, 954, 93
Asaba, S., Ichiki, K., & Tashiro, H. 2016, PhRvD, 93, 023518
Birnboim, Y., & Dekel, A. 2003, MNRAS, 345, 349
Bovino, S., Latif, M. A., Grassi, T., & Schleicher, D. R. G. 2014, MNRAS, 441, 2181
Bovy, J., & Dvorkin, C. 2013, ApJ, 768, 70
Burkhart, B. 2018, ApJ, 863, 118
Burkhart, B., & Mocz, P. 2019, ApJ, 879, 129
Cain, C., D'Aloisio, A., Iršič, V., McQuinn, M., & Trac, H. 2020, ApJ, 898, 168
Chen, K.-J., Ho, M.-Y., & Tung, P.-C. 2025, ApJL, 988, L67
Chiaki, G., & Wise, J. H. 2019, MNRAS, 482, 3933
Chiou, Y. S., Naoz, S., Marinacci, F., & Vogelsberger, M. 2018, MNRAS, 481, 3108
Clark, P. C., Glover, S. C. O., & Klessen, R. S. 2008, ApJ, 672, 757
Clark, P. C., Glover, S. C. O., Klessen, R. S., & Bromm, V. 2011, ApJ, 727, 110
Dalal, N., Pen, U., & Seljak, U. 2010, JCAP, 11, 007
Druschke, M., Schauer, A. T. P., Glover, S. C. O., & Klessen, R. S. 2018, MNRAS, 481, 3266
Falceta-Gonçalves, D., Kowal, G., Falgarone, E., & Chian, A. C. L. 2014, NPGeo, 21, 587
Fernandez, R., Bryan, G. L., Haiman, Z., & Li, M. 2014, MNRAS, 439, 3798
Fialkov, A. 2014, IJMPD, 23, 1430017
Fialkov, A., Barkana, R., Tseliakhovich, D., & Hirata, C. M. 2012, MNRAS, 424, 1335
Gnedin, N. Y. 2000, ApJ, 542, 535
Greif, T. H., Bromm, V., Clark, P. C., et al. 2012, MNRAS, 424, 399
Greif, T. H., Johnson, J. L., Klessen, R. S., & Bromm, V. 2008, MNRAS, 387, 1021
Greif, T. H., White, S. D. M., Klessen, R. S., & Springel, V. 2011, ApJ, 736, 147
Harris, C. R., Millman, K. J., van der Walt, S. J., et al. 2020, Natur, 585, 357
Hegde, S., & Furlanetto, S. R. 2023, MNRAS, 525, 428
Higashi, S., Susa, H., & Chiaki, G. 2021, ApJ, 915, 107
Hirano, S. 2025, MNRAS, 540, 331
Hirano, S., Hosokawa, T., Yoshida, N., & Kuiper, R. 2017, Sci, 357, 1375
Hirano, S., Hosokawa, T., Yoshida, N., Omukai, K., & Yorke, H. W. 2015, MNRAS, 448, 568
Hirano, S., Hosokawa, T., Yoshida, N., et al. 2014, ApJ, 781, 60
Hirano, S., Yoshida, N., Sakurai, Y., & Fujii, M. S. 2018, ApJ, 855, 17
Ho, K. W., Yuen, K. H., & Lazarian, A. 2023, MNRAS, 521, 230
Ho, M.-Y., Chen, K.-J., & Tung, P.-C. 2025, arXiv:2505.23768
Hummel, J. A., Stacy, A., & Bromm, V. 2016, MNRAS, 460, 2432
Hummel, J. A., Stacy, A., Jeon, M., Oliveri, A., & Bromm, V. 2015, MNRAS, 453, 4136
Hunter, J. D. 2007, CSE, 9, 90
Jaura, O., Glover, S. C. O., Wollenberg, K. M. J., et al. 2022, MNRAS, 512, 116
Kang, H., Ryu, D., Cen, R., & Ostriker, J. P. 2007, ApJ, 669, 729
Kereš, D., Katz, N., Weinberg, D. H., & Davé, R. 2005, MNRAS, 363, 2
Kiyuna, M., Hosokawa, T., & Chon, S. 2023, MNRAS, 523, 1496
Klessen, R. S., & Glover, S. C. O. 2023, ARA&A, 61, 65
Krumholz, M. R., & McKee, C. F. 2005, ApJ, 630, 250
Kulkarni, M., Visbal, E., & Bryan, G. L. 2021, ApJ, 917, 40

Lake, W., Grudić, M. Y., Naoz, S., et al. 2025, ApJL, 985, L6
Lake, W., Naoz, S., Chiou, Y. S., et al. 2021, ApJ, 922, 86
Lake, W., Naoz, S., Burkhart, B., et al. 2023a, ApJ, 943, 132
Lake, W., Naoz, S., Marinacci, F., et al. 2023b, ApJL, 956, L7
Lake, W., Williams, C. E., Naoz, S., et al. 2024, ApJ, 973, 115
Larson, R. B. 1981, MNRAS, 194, 809
Latif, M. A., Niemeyer, J. C., & Schleicher, D. R. G. 2014a, MNRAS, 440, 2969
Latif, M. A., Schleicher, D. R. G., & Schmidt, W. 2014b, MNRAS, 440, 1551
Latif, M. A., Whalen, D. J., Khochfar, S., Herrington, N. P., & Woods, T. E. 2022, Natur, 607, 48
Lazarian, A., & Beresnyak, A. 2006, MNRAS, 373, 1195
Lazarian, A., Xu, S., & Hu, Y. 2023, FrASS, 10, 1154760
Liu, B., Gurian, J., Inayoshi, K., et al. 2024, MNRAS, 534, 290
Furlanetto, S. R., & Loeb, A. 2013, ApJ, 611, 642
Long, H., Givans, J. J., & Hirata, C. M. 2022, MNRAS, 513, 117
Maio, U., Koopmans, L. V. E., & Ciardi, B. 2011, MNRAS, 412, L40–L44
McQuinn, M., & O'Leary, R. M. 2012, ApJ, 760, 3
Muñoz, J. B. 2019, PhRvD, 100, 063538
Nakazato, Y., Chiaki, G., Yoshida, N., et al. 2022, ApJL, 927, L12
Naoz, S., & Barkana, R. 2005, MNRAS, 362, 1047
Naoz, S., & Barkana, R. 2007, MNRAS, 377, 667
Naoz, S., & Narayan, R. 2013, PhRvL, 111, 051303
Naoz, S., & Narayan, R. 2014, ApJL, 791, L8
Naoz, S., Yoshida, N., & Gnedin, N. Y. 2012, ApJ, 747, 128
Naoz, S., Yoshida, N., & Gnedin, N. Y. 2013, ApJ, 763, 27
Nebrin, O., Giri, S. K., & Mellema, G. 2023, MNRAS, 524, 2290
O'Leary, R. M., & McQuinn, M. 2012, ApJ, 760, 4
Park, H., Ahn, K., Yoshida, N., & Hirano, S. 2020, ApJ, 900, 30
Park, H., Shapiro, P. R., Ahn, K., Yoshida, N., & Hirano, S. 2021, ApJ, 908, 96
Popa, C., Naoz, S., Marinacci, F., & Vogelsberger, M. 2016, MNRAS, 460, 1625
Prieto, J., Jimenez, R., & Martí, J. 2012, MNRAS, 419, 3092
Prieto, J., Padoan, P., Jimenez, R., & Infante, L. 2011, ApJL, 731, L38
Riaz, R., Bovino, S., Vanaverbeke, S., & Schleicher, D. R. G. 2018, MNRAS, 479, 667
Riaz, R., Schleicher, D. R. G., Bovino, S., Vanaverbeke, S., & Klessen, R. S. 2023, MNRAS, 518, 4895
Richardson, M. L. A., Scannapieco, E., & Thacker, R. J. 2013, ApJ, 771, 81
Sadanari, K. E., Omukai, K., Sugimura, K., Matsumoto, T., & Tomida, K. 2024, PASJ, 76, 823
Safranek-Shrader, C., Agarwal, M., Federrath, C., et al. 2012, MNRAS, 426, 1159
Schaal, K., & Springel, V. 2015, MNRAS, 446, 3992
Schaal, K., Springel, V., Pakmor, R., et al. 2016, MNRAS, 461, 4441
Schauer, A. T. P., Glover, S. C. O., & Klessen, R. S. 2017, MmSAI, 88, 702
Schauer, A. T. P., Glover, S. C. O., Klessen, R. S., & Ceverino, D. 2019, MNRAS, 484, 3510
Schauer, A. T. P., Glover, S. C. O., Klessen, R. S., & Clark, P. 2021, MNRAS, 507, 1775
Seljak, U., & Zaldarriaga, M. 1996, ApJ, 469, 437
Sharda, P., & Menon, S. H. 2025, MNRAS, 540, 1745
Slepian, Z., & Eisenstein, D. J. 2015, MNRAS, 448, 9
Smith, B. D., Bryan, G. L., Glover, S. C. O., et al. 2017, MNRAS, 466, 2217
Springel, V., White, S. D. M., Tormen, G., & Kauffmann, G. 2001, MNRAS, 328, 726
Stacy, A., Bromm, V., & Loeb, A. 2011, ApJL, 730, L1
Stacy, A., Greif, T. H., & Bromm, V. 2010, MNRAS, 403, 45
Stacy, A., Greif, T. H., & Bromm, V. 2012, MNRAS, 422, 290
Stacy, A., McKee, C. F., Lee, A. T., Klein, R. I., & Li, P. S. 2022, MNRAS, 511, 5042
Sugimura, K., Matsumoto, T., Hosokawa, T., Hirano, S., & Omukai, K. 2023, ApJ, 959, 17
Susa, H., Hasegawa, K., & Tominaga, N. 2014, ApJ, 792, 32
Tanaka, T. L., & Li, M. 2014, MNRAS, 439, 1092
Tang, C.-Y., & Chen, K.-J. 2024, MNRAS, 529, 4248
Tseliakhovich, D., Barkana, R., & Hirata, C. M. 2011, MNRAS, 418, 906
Tseliakhovich, D., & Hirata, C. 2010, PhRvD, 82, 083520
Turk, M. J., Smith, B. D., Oishi, J. S., et al. 2011, ApJS, 192, 9
Uysal, B., & Hartwig, T. 2023, MNRAS, 520, 3229
Virtanen, P., Gommers, R., Oliphant, T. E., et al. 2020, NatMe, 17, 261
Visbal, E., Barkana, R., Fialkov, A., Tseliakhovich, D., & Hirata, C. M. 2012, Natur, 487, 70
Vogelsberger, M., Marinacci, F., Torrey, P., & Puchwein, E. 2020, NatRP, 2, 42
Weinberger, R., Springel, V., & Pakmor, R. 2020, ApJS, 248, 32
Williams, C. E., Lake, W., Naoz, S., et al. 2024, ApJL, 960, L16
Williams, C. E., Naoz, S., Lake, W., et al. 2023, ApJ, 945, 6
Williams, C. E., Naoz, S., Lake, W., et al. 2025, ApJ, 990, 135
Wise, J. H., & Abel, T. 2007, ApJ, 665, 899
Wollenberg, K. M. J., Glover, S. C. O., Clark, P. C., & Klessen, R. S. 2020, MNRAS, 494, 1871
Yoo, J., Dalal, N., & Seljak, U. 2011, JCAP, 7, 18
Yoshida, N., Abel, T., Hernquist, L., & Sugiyama, N. 2003, ApJ, 592, 645
Yoshida, N., Omukai, K., & Hernquist, L. 2007, ApJL, 667, L117
Yoshida, N., Omukai, K., Hernquist, L., & Abel, T. 2006, ApJ, 652, 6
Yuen, K. H., Ho, K. W., Law, C. Y., & Chen, A. 2024, RvMPP, 8, 21